Experimental validation of flow models for a rigid vocal tract replica

Annemie Van Hirtum,[a] Xavier Pelorson, and Olivier Estienne
GIPSA-lab, UMR CNRS 5216, Grenoble University, F-38031 Grenoble Cedex 1, France

Hélène Bailliet
Institut P' CNRS, Université de Poitiers, ENSMA, Département Fluides Thermique Combustion, ESIP, Bâtiment K, Campus Sud, 40 avenue du recteur Pineau, F-86022 Poitiers Cedex, France

(Received 17 March 2010; revised 5 August 2011; accepted 8 August 2011)

Flow through the vocal tract is studied through an *in vitro* rigid replica for different geometrical configurations and steady flow conditions with bulk Reynolds numbers $\mathrm{Re} < 15\,000$. The vocal tract geometry is approximated by two consecutive obstacles, representing "tongue" and "tooth," in a rectangular channel of fixed length. For the upstream tongue obstacle with fixed constriction degree (81%) the streamwise position is varied and for the downstream obstacle the constriction degree is varied from 0% up to 96%. Different upstream pressures are considered for each geometrical configuration. Point pressure measurements at three fixed locations along the channel are experimentally assessed. In addition, the volume airflow rate is measured. The pressure distribution is estimated with a one-dimensional flow model, and the effects of different corrections to a laminar irrotational flow are assessed. The model outcome is validated against experimental data. Depending on the geometrical configuration, the best model accuracy is obtained by accounting for viscosity (needed for constriction degrees at the tooth that are small, i.e.,$\leq 58\%$, or very large, i.e., $\geq 96\%$), a sudden constriction (large gap between both constrictions), or a bending geometry (narrow gap between both constrictions). Best overall model errors vary between 4% and 30% for all assessed geometrical configurations in cases where a tongue obstacle is present.
 [DOI: 10.1121/1.3631631]

PACS number(s): 43.70.Bk, 43.70.Jt [CHS] Pages: 2128–2138

I. INTRODUCTION

Research on physical modeling of human speech production is mainly concentrated on voiced sound production. In particular, simplified quasi-one-dimensional flow models are commonly used to describe the glottal flow driving the auto-oscillation of the vocal folds (e.g., Ishizaka and Flanagan, 1972; Lous *et al.*, 1998; Ruty *et al.*, 2007). As a consequence, the validation of quasi-one-dimensional flow models is extensively studied on simplified rigid mechanical models of the glottis containing the vocal folds (e.g., Pelorson *et al.*, 1994; Barney *et al.*, 1999; Cisonni *et al.*, 2008). Simplified mechanical geometries with a limited number of geometrical parameters are used to avoid experimental results which can not be reliably interpreted.

Similarly, a necessary step to describe unvoiced fricative sound production is to characterize the flow through the vocal tract downstream the glottis. Aerodynamic and aeroacoustic principles have been introduced in speech production studies dealing with fricatives since Fant (1960). This pioneering work has been further developed by experimental as well as modeling studies (e.g., Shadle, 1985; Sinder, 1999; Adachi and Honda, 2003; Howe and McGowan, 2005; Krane, 2005; Shadle *et al.*, 2008). An extensive and systematic study of flow through the vocal tract downstream of the glottis for configurations relevant for unvoiced sound production is lacking as recently pointed out (Howe and McGowan, 2005; Bodony, 2005). Therefore, a systematic comparison of measurements on simplified mechanical vocal tract models to physical flow models is necessary to gain insight in the observed flow regime. In addition, it is of interest to determine if the simplified quasi-one-dimensional flow model approach, commonly applied to glottal flow, can be extended to model the mean flow behavior in the vocal tract during fricative production.

The underlying mechanism of sibilant fricative sound production is generally described as *noise produced due to the interaction of a turbulent jet, issued from a constriction somewhere in the vocal tract, with a downstream wall or obstacle*. Consequently, the position and shape of articulators like tongue and teeth determine the generation and development of the jet as well as its downstream interaction with a wall or obstacle as is indeed observed on human speakers (Narayanan *et al.*, 1995; Runte *et al.*, 2001). It follows that experimental and simulation studies have been performed in order to characterize and quantify the influence of "articulators" position and shape on the sound produced (Shadle, 1985, 1991; Ramsay, 2008; Nozaki *et al.*, 2005). Nevertheless, the previous studies focus on the acoustics of fricative noise production and not on the flow. In fact, there are few studies that use flow data to provide a systematic characterization issuing from configurations relevant to human fricative production, i.e., moderate Reynolds Re numbers covering the range $2000 < \mathrm{Re} < 10^4$ (Stevens, 1998) and low Mach number M (Howe and McGowan, 2005; Bodony, 2005).

[a]Author to whom correspondence should be addressed. Electronic mail: annemie.vanhirtum@gipsa-lab.grenoble-inp.fr.

 0001-4966/2011/130(4)/2128/11/$30.00

Recently, single sensor anemometry was used to characterize the spatial velocity distribution issued from an extended conical diffuser (Re = 7350) (Van Hirtum *et al.*, 2009b). The data validated self-similar flow models of jet development, which can be applied to model the jet through the constriction between the tongue and the palatal plane, although no obstacle was considered. In addition, flow development through a rectangular channel with a teeth-shaped obstacle inserted was studied by comparing simulated and measured velocity data in the near field downstream of the teeth edge (Re = 4000) (Van Hirtum *et al.*, 2010), although no jet formation upstream of the obstacle was considered. Besides the limitation of Van Hirtum *et al.* (2009b, 2010) to one Reynolds number, it is evident that no geometry representing jet formation followed by a downstream obstacle was considered. Therefore, a systematic study of flow data for such a geometry typical for sibilant fricative production is lacking.

A simplified rigid mechanical vocal tract replica, characterized by a few geometrical parameters, is described in Shadle (1985, 1991). In the current study, a rectangular rigid mechanical replica, inspired by the one presented in Shadle (1985, 1991), is proposed in order to mimic the vocal tract geometry combining a constriction followed by a downstream obstacle. The replica consists of a constricted portion between the tongue and the "palatal plane" upstream of an obstacle representing a tooth for which the constriction can be varied. Its dimensions are taken to be relevant to the human physiology of an "average" male adult vocal tract (Daniloff *et al.*, 1980; Hirano *et al.*, 1987; Narayanan *et al.*, 1995; Runte *et al.*, 2001; Stevens, 1998; Rudolph *et al.*, 1998; Magne *et al.*, 2003). The gap between the constricted vocal tract portion and the obstacle as well as the constriction degree at the obstacle are systematically varied. In addition, the flow conditions are varied so that the relevant range of Reynolds numbers is experimentally assessed. The flow is characterized by measuring the volume flow rate and performing point pressure measurements at different positions along the replica.

These data are compared to the results of one-dimensional flow model approach commonly used to describe the mean flow in physical models of phonation in order to validate the degree to which the models are suitable to describe the flow through the entire upper airway from the larynx up to the lips. Since it is obvious that the flow is too complex to be represented by a laminar flow model, assumed in Bernoulli's equation, several *ad hoc* corrections are assessed to describe the influence of vorticity and turbulence on the mean flow. The flow model outcome is particularly validated for (1) variation of the distance between jet and obstacle as well as (2) the constriction degree at the obstacle.

II. ONE-DIMENSIONAL FLOW MODELS

Considering a rectangular channel with two constrictions as schematically shown in Fig. 1, the total pressure difference ΔP_{tot} is given as

$$\Delta P_{\text{tot}} = \Delta P_1 + \Delta P_2 + \Delta P_3 + \Delta P_4 + \Delta P_5, \tag{1}$$

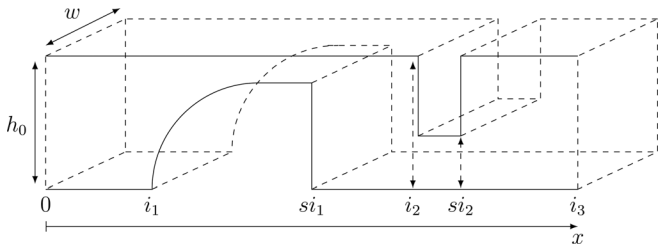

FIG. 1. Schematic overview of the geometry: rectangular channel with fixed width w characterized by height variation $h(x)$. The unconstricted channel height is denoted h_0 and two constrictions are inserted spanning the intervals $[i_1\ si_1]$ and $[i_2\ si_2]$. The x-axis indicates the main flow direction.

with

$$\begin{aligned}
\Delta P_1 &= P(x=0) - P(x=i_1),\\
\Delta P_2 &= P(x=i_i) - P(x=si_1),\\
\Delta P_3 &= P(x=si_1) - P(x=i_2),\\
\Delta P_4 &= P(x=i_2) - P(x=si_2),\\
\Delta P_5 &= P(x=si_2) - P(x=i_3).
\end{aligned}$$

It is assumed that no pressure loss occurs in the uniform inlet portion so that $P_0 = P(x=0) = P(x=i_1)$ and $\Delta P_1 = 0$. The pressure losses ΔP_i in the remaining portions with varying area $A_{i,si}$, with subscript i denoting the upstream position and subscript si the downstream position, can be modeled by application of a combination of terms from which the pressure distribution $p(x)$ follows immediately (Blevins, 1992; Kundu, 1990; White, 1991; Cisonni *et al.*, 2008; Van Hirtum *et al.*, 2009a). In the following the different terms are explained and equations are given. Assuming a simplified one-dimensional quasi-stationary incompressible and irrotational flow described by the stationary Bernoulli's equation given in (2) and denoted ΔP_i^{ber},

$$\begin{aligned}
\Delta P_i^{\text{ber}} &= Q^2 \frac{\rho}{2}\left(\frac{1}{A_{si}^2} - \frac{1}{A_i^2}\right),\\
&= Q^2 \frac{\rho}{2}\frac{1}{A_i^2}\left(\frac{A_i^2}{A_{si}^2} - 1\right),
\end{aligned} \tag{2}$$

with volume flux Q and mean air density ρ.

Several corrections to (2) can be considered due to flow separation, viscosity, or downstream pressure recovery. Since steady flow conditions are considered no correction for unsteady flow is necessary. For the geometry shown in Fig. 1, flow separation is assumed to occur at locations x_{si1} and x_{si2} regardless upstream pressure P_0 or volume flow rate Q so that the position of flow separation is fixed and no correction for position change is needed. Viscous losses, on the contrary, are known to be important in case of low Reynolds numbers, i.e., low velocity or small height $h(x)$. Therefore, the Bernoulli equation is corrected for viscosity by adding a viscous pressure loss term (3) denoted ΔP_i^{visc} derived from a fully developed viscous Poiseuille profile as outlined in Appendix A,

$$\Delta P_i^{\text{visc}} = Q\frac{-12\mu}{w}\int_{x_i}^{x_{si}} \frac{dx}{h(x)^3}, \tag{3}$$

with dynamic viscosity coefficient μ.

So far, pressure recovery by flow reattachment upstream the flow separation point is neglected. In Ishizaka and Flanagan (1972) the pressure recovery is estimated by evaluating the quasi steady momentum equation. The resulting expression (4) describes the pressure recovery as a portion of the Bernoulli loss term (2):

$$\Delta P_i^{\exp} = Q^2 \frac{\rho}{2} \frac{1}{A_i^2} \left[\left(\frac{A_i^2}{A_{si}^2} - 1 \right) + \left(1 - \frac{A_i}{A_{si}} \right) \right] = Q^2 \frac{\rho}{2} \left[\frac{-2}{A_i A_{si}} \left(1 - \frac{A_i}{A_{si}} \right) \right]. \quad (4)$$

The magnitude of the recovery depends on the area ratio A_i/A_{si} at the position of flow separation A_i and the expanded area A_{si} downstream the constriction. It is clear that (4) assumes a uniform flow profile over area A_{si} so that the pressure recovery becomes proportional to $1 - (A_i/A_{si})$.[2] On the other hand zero pressure recovery is expected in case a narrow jet flow is assumed to be maintained, so that $A_{si} = A_i$ and the loss term becomes zero since $(1 - A_i/A_{si}) = 0$, corresponding to not taking Eq. (4) into account.

Alternatively to the extreme cases of no recovery or uniform flow, an intermediate value for the pressure recovery is expected in case of an expanding jet geometry to which (2) can be applied. A geometrical correction for jet expansion is easily obtained by applying an expansion angle θ_{jet} to the uniform narrow jet as

$$A_{\text{jet}} = [h_i + C_{\text{jet}} \tan(\theta_{\text{jet}})(x_{si} - x_i)]w, \quad (5)$$

with expansion angle $\theta_{\text{jet}} \sim 4.2°$ and model constant C_{jet} set to 1 or 2 accounting for one-side or two-side geometrical expansion of a two-dimensional jet (Kundu, 1990; White, 1991). The constricted portion indicated $[i_2, si_2]$ in Fig. 1 can be seen as a thin square-edged contraction for which separation might occur depending on the Reynolds number at the leading edge, $x = i_2$, instead of the trailing edge, $x = si_2$. In case separation occurs, the flow through the constriction is accelerated and a pressure loss occurs as reported in (7) where C_{con} can be seen as an discharge coefficient whose value can be estimated from geometrical considerations (6), (8) or as an *ad hoc* orifice coefficient (7) Blevins (1992).

$$\Delta P_i^{\text{con}} = Q^2 \frac{\rho}{2} \frac{1}{A_{si}^2} \left[\left(1 - \frac{A_{si}^2}{A_i^2} \right) + \frac{1}{2} \left(1 - \frac{A_{si}}{A_i} \right) \right] = Q^2 \frac{\rho}{2} \frac{1}{A_{si}^2} \left(1 - \frac{A_{si}^2}{A_i^2} \right) \left(1 + \frac{1}{2} \left[1 + \frac{A_{si}}{A_i} \right]^{-1} \right), \quad (6)$$

$$= Q^2 \frac{\rho}{2} \frac{1}{A_{si}^2} \left(1 - \frac{A_{si}^2}{A_i^2} \right) \frac{1}{C_{\text{con}}^2}, \quad C_{\text{con}} < 1, \quad (7)$$

$$C_{\text{con}} = \left[1 + \frac{1}{2} \left(1 + \frac{A_{si}}{A_i} \right)^{-1} \right]^{-1/2}. \quad (8)$$

Expressions (2)–(7) assume the main flow direction to be along the x axis. However, when the distance between the downstream and upstream constriction is reduced, the channel geometry seen by the flow presents two 90° turns, one at the entrance and one at the exit of the gap between the two obstacles. Therefore, the main flow direction following the x-direction along both constrictions is likely to be perpendicular to the x-direction inside the gap between both constrictions. In this case, the geometry can be seen as a sharp 90° bend for which the pressure loss can be described with in which the coefficient C_{ben} is either estimated from the volume flow rate and the geometry or chosen as an *ad hoc* bending discharge coefficient Blevins (1992).

$$\Delta P_i^{\text{ben}} = Q^2 \frac{\rho}{2} \left[\frac{1.1}{A_{si}^2} \left(\frac{2 \times 10^5}{\text{Re}_D} \right)^{0.2} \right], \quad (9)$$

$$= Q^2 \frac{\rho}{2} \left[\frac{C_{\text{ben}}}{A_{si}^2} \right], \text{Re}_D < 2 \times 10^5 \rightarrow C_{\text{ben}} > 1.1, \quad (10)$$

$$C_{\text{ben}} = 1.1 \left(\frac{2 \times 10^5}{\text{Re}_D} \right)^{0.2}, \quad (11)$$

with Re_D denoting the Reynolds number based on the corresponding hydraulic diameter, which for a rectangular area with width w, $A = wh$, is defined as $\text{Re}_D = (2\rho Q)/[\mu(w + h)]$. For the range of Re_D under consideration, $0 < \text{Re}_D < 19\,000$, the coefficient C_{ben} is $1.1 < C_{\text{ben}}$ with a typical value yielding $C_{\text{ben}} \approx 2.2$.

Alternatively, a change in flow direction in the narrowed portion between both constrictions can be simply accounted for by exchanging height and length in this section of the channel and applying the previous mentioned terms, (2)–(7), in order to determine the pressure distribution $p(x)$ along the main flow direction.

Except for the viscous loss term (3), the pressure differences ΔP_i in expressions (2)–(10), for known volume airflow velocity, are of the form $\Delta P_i = f(Ai, A_{si})$ which, in case of a channel with fixed width w, reduces further to $\Delta P_i = f(h_i, h_{si})$. The relative importance of resulting pressure differences ΔP_i normalized with respect to a positive real power $b > 0$ of volume flow rate Q,

$$\Delta P_i / Q^b = f(h_i, h_s) \text{ and } b \in \mathbb{R}_0^+, \quad (12)$$

with $\mathbb{R}_0^+ = \{x \in \mathbb{R} | x > 0\}$ is illustrated in Fig. 2 for $b = 2$ and $C_{\text{ben}} = 2.2$. Two different upstream heights h_i are illustrated, i.e., $h_i = 16$ and $h_i = 3$ mm. The values of h_i and h_{si} are chosen in the range of magnitudes relevant for the current study. Illustrated pressure losses are normalized with respect to the bending term (10) for $h_{si} = 0.6$ mm, since $\Delta P_i^{\text{ben}}(h_{si} = 0.6) = c_1$ with c_1 a constant value independent of h_i. Consequently the applied normalization is independent of h_i which favors interpretation and comparison between both assessed h_i values. Figure 2(a) and 2(b) illustrate the resulting pressure losses in case h_{si} is varied in the intervals [0.6 3] and [3 16] mm, respectively. For a given volume airflow rate and h_{si} in the range [0.6 3] mm, i.e., $h_{si} \neq h_i$, the relative pressure losses obtained from (2), (4), (7), and (10) are highly dependent on h_{si} as can be seen from Fig. 2(a).

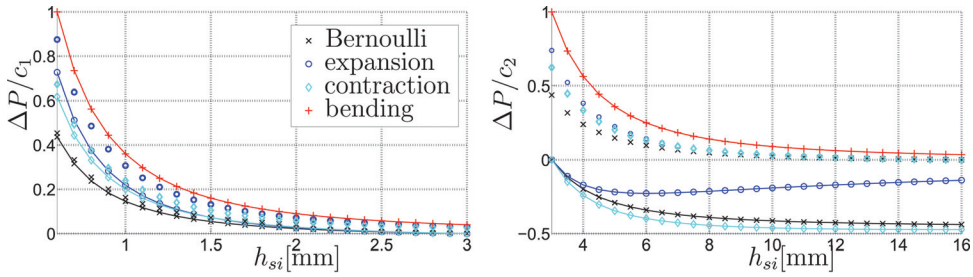

(a)h_{si} 0.6 to 3mm (b)h_{si} 3 to 16mm

FIG. 2. (Color online) Relative importance of the pressure difference $\Delta P/Q^2 = f(hi,h_{si})$ with f defined from (2) (× Bernoulli), (4) (○ expansion), (7) (◊ contraction) and (10) (+ bending), respectively, for upstream heights $h_i = 16$ mm (no line) and $h_i = 3$ mm (full line): a) $h_{si} \in$ [0.6 3] mm normalized with $\Delta P^{\text{ben}}(h_{si} = 0.6) = c_1$ and b) $h_{si} \in$ [3 16] mm normalized with $\Delta P^{\text{ben}}(h_{si} = 3) = c_2$.

The relative difference between the terms for a given h_{si} is seen to decrease from 55% to 5% as h_{si} increases from 0.6 to 3mm. As expected, application of (4), (7), or (10) increases the pressure loss compared to the Bernoulli term expressed in (2). In order to consider the different contributions to the pressure losses, all terms are presented in Fig. 2(a) regardless their physical relevance. In particular, the expansion term (4) results in an intermediate pressure loss compared to the other loss terms although of course no geometrical expansion is present since $h_i > h_{si}$ for $h_i \in$ [3 16] mm. The relative influence of h_i for $h_i > h_{si}$ is seen to be less than 10%, except for the unphysical expansion term for which the difference is less than 20%, for the whole range [0.6 3] mm and is decreasing as the ratio h_{si}/h_i increases. For $h_i = 3$ mm, the ratio $h_{si}/h_i \to 1$ as $h_{si} \to 3$, and consequently, all terms, except the Bending term, become 0 in this limit. For $h_i = 16$ mm, all terms remain > 0.

Pressure differences for $h_{si} \in$ [3 16] mm are illustrated in Fig. 2(b). As in Fig. 2(a), physically meaningless terms are shown in order to illustrate the model behavior completely, i.e., the expansion term (4) for $h_i = 16$ mm and the contraction term (7) for $h_i = 3$ mm. Pressure values are normalized with respect to the bending term (10) obtained for $h_{si} = 3$ mm, i.e., $\Delta P_i^{\text{ben}}(h_{si} = 3) = c_2$ with c_2 a constant value independent of h_i. For $h_i = 16$ mm the condition $h_{si}/h_i < 1$ is still valid and therefore the observations described on Fig. 2(a) can be extended to the relative pressure losses illustrated in Fig. 2(b). The relative difference decreases as h_{si} approaches $h_i = 16$ mm, in which case all terms except the Bending term (10) go to 0. For $h_i = 3$ mm, different observations can be made since $h_{si}/h_i > 1$ for $h_{si} \in$ [3 16] mm. For $h_{si}/h_i > 1$ Bernoulli (2) and Expansion (4) result in pressure recovery with respect to the upstream pressure, i.e., $\Delta P < 0$. Furthermore, it is easily derived from (4) that a maximum pressure recovery occurs for $h_{si} = 2h_i$. This is illustrated in Fig. 2(a) where a maximum for the expansion term is indeed observed at $h_{si} = 6$ mm for $h_i = 3$ mm. From (3) and (5) it is seen that besides a dependence on $h(x)$, the pressure difference induced by (3) as well as the importance of the geometrical jet expansion (5) increases as the streamwise extent increases.

III. RIGID *IN VITRO* REPLICA AND EXPERIMENTAL SETUP

The rigid *in vitro* replica consists of two constrictions, C_1 and C_2, inserted in a uniform rectangular channel as schematically depicted in Fig. 1 and detailed in Fig. 3. The unconstricted channel has length $L_0 = 180$ mm, height $h_0 = 16$ mm, width $w = 21$ mm, and aspect ratio $w/h_0 = 1.3$. The shape of both constrictions C_1 and C_2 is fixed. Their lengths in the x-direction yield $l_1 = 30$ mm for C_1 and $l_2 = 3$ mm for C_2. The aperture h_1 is fixed to 3 mm, which corresponds to a constriction degree of 81%. The distance of the trailing edge of C_2 to the channel exit, L_2, is fixed to 6 mm. The distance of the trailing edge of C_1 with respect to the channel exit, L_1, can be varied as well as aperture height h_2 of constriction C_2. Therefore, besides the inlet height h_0, the

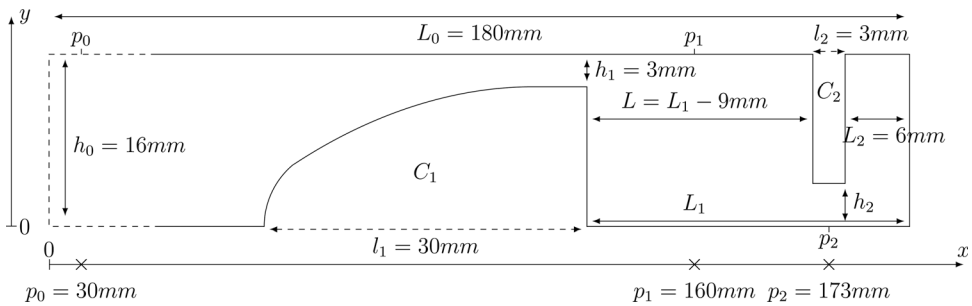

FIG. 3. Two dimensional schema of rigid *in vitro* replica: rectangular channel with fixed unconstricted height $h_0 = 16$ mm, uniform width $w = 21$ mm and total length $L_0 = 180$ mm containing two constrictions C_1 and C_2. The main streamwise direction corresponds to the x axis. The constricted portions C_1 and C_2 has streamwise lengths $l_1 = 30$ mm and $l_2 = 3$ mm, respectively. The minimum aperture height of C_1 is indicated h_1 and of C_2 is denoted h_2. The distance between the channel exit and the trailing edge of C_1 and C_2 is denoted L_1 and L_2, respectively. The distance between the trailing edge of C_1 and the leading edge of C_2 is denoted L. The geometrical parameters yield $L_2 = 6$ mm and $h_1 = 3$ mm. The geometrical parameters L_1 and h_2 can be varied. Three pressure taps are present at downstream positions $p_0 = 30$ mm, $p_1 = 160$ mm, and $p_2 = 173$ mm.

TABLE I. Summary of 37 experimentally assessed geometrical conditions illustrated in Fig. 4. All used combinations of (L_1, h_2) are accounted for by combining 6 values listed for L_1 in (a) with 6 aperture values h_2 at the obstacle given in (b). Resulting values for the gap between both constrictions $L = L_1 - 9$ mm and associated constriction degrees [%] due to L, $1 - L/h_0$, and the obstacle aperture h_2, $1 - h_2/h_0$, are indicated. Note that the constriction degree at h_1 due to C_1 is fixed to 81% whenever C_1 is present. Absence of C_1 is denoted '–' in subtable (a). In addition, to the 36 (L_1, h_2)-combinations of (a) and (b), a no-front cavity case without obstacle ($L_1 = 1$mm, $h_2 = /$) is considered.

(a) L_1 and derived variables

L_1 [mm]	- (no C_1)	33	25	19	14	12
L [mm]	- (no C_1)	24	16	10	5	3
1 - L/h_0 [%]	0 (no C_1)	0	0	38	69	81

(b) h_2 and derived variables

h_2 [mm]	16 (no C_2)	6.8	5.5	2.6	1.5	0.6
1 - h_2/h_0 [%]	0 (no C_2)	58	66	84	91	96

TABLE II. Comparison of typical values related to the vocal tract during fricative production and the replica (Daniloff *et al.*, 1980; Hirano *et al.*, 1987; Narayanan *et al.*, 1995; Runte *et al.*, 2001; Stevens, 1998; Rudolph *et al.*, 1998; Magne *et al.*, 2003). The assessed values for the experimentally varied geometrical parameters, h_2 and L, are further detailed in Table I.

Quantity	Symbol	On human	On replica
Vocal tract height	h_0	10–20 mm	16 mm
Vocal tract width	w	15–25 mm	21 mm
Vocal tract length	L_0	150–190 mm	180 mm
Minimum aperture at the tongue	h_1	1–4 mm	3 mm
Length of teeth	l_2	1–2 mm	3 mm
Distance between teeth and lips	L_2	$1.7 \times l_2$	6 mm
Minimum aperture at the teeth	h_2	1–2 mm	0.6–16 mm
Distance between tongue constriction and teeth	L	5–15 mm	3–24 mm
Reynolds number	Re	$2000 < \mathrm{Re} < 10^4$	$\mathrm{Re} < 15000$

pressure distribution is determined by the set of geometrical parameters $\{h_1, L_1, h_2\}$ among which L_1 and h_2 can be varied. In order to validate the pressure drop, three pressure taps are assessed at positions $p_0 = 30$ mm, $p_1 = 160$ mm, and $p_2 = 173$ mm from the channel inlet. The position of the pressure taps is fixed to prevent leakage.

All combinations of $\{L_1, h_2\}$, for which the values are summarized in Table I, are experimentally assessed. The cases $h_2 = 16$ mm and $L_1 = 1$ mm correspond to "no-tooth" configurations. Since the position of the pressure tap p_1 is fixed, p_1 is either situated in the gap between C_1 and C_2 for large L_1 or along C_1 in case L_1 is small. The successive different downstream positions of C_1, given in Table I, respectively, correspond to a trailing edge position situated either at 13 and 5 mm downstream of p_1 or at 1, 6, 8, or 19 mm upstream of p_1. An overview of the different trailing edge positions is depicted in Fig. 4. A comparison between experimental replica values and typical values observed on *in vivo* speakers is given in Table II.

Next, the *in vitro* replica is mounted into a suitable experimental setup. Air is supplied by a compressor (Copco GA7). The compressor is connected by a tube with diameter 1 cm to a pressure regulator (Norgren type 11-818-987) and a downstream manual valve in order to provide steady flow. A tube with diameter 1 cm connects the manual valve to a massflowmeter (TSI 4001), which is connected further downstream to a pressure tank of 0.073 m.[3] The rectangular pressure tank of dimensions $360 \times 500 \times 400$ mm ($x \times y \times z$) is tapered with acoustical foam (SE50AL-ML). The *in vitro* replica described before is directly mounted to the pressure tank. The upstream pressure P_0, the intermediate pressure P_1, 11 mm upstream of C_2, and pressure P_2, at constriction C_2, are measured with pressure transducers (Kulite XCS-093) at the pressure taps p_0, p_1, and p_2 shown in Figs. 3 and 4. The volume flow rate Q is measured using the massflowmeter (TSI 4001) upstream of the pressure tank.

IV. DATA AND OPTIMAL DATA APPROXIMATION

Measured point pressures and volume flow rates for imposed flow and geometrical conditions are discussed in Sec. IV A. In Sec. IV B, measured data are analyzed by means of an *ad hoc* estimation of the coefficients for a parametrical function derived from (2). A data-based optimization approach enables us to determine if such a simple mathematical expression is able to explain the data. The resulting error indicates a minimum value and is therefore a reference for the model validation presented in Sec. V. In particular, the influence of the geometrical parameters on the accuracy of predictions with the parametrical function is assessed.

A. Experimental volume flow and pressure data

The geometrical configurations depicted in Fig. 3 and Fig. 4 are assessed for upstream pressures $P_0 \leq 4000$ Pa. The associated bulk Reynolds numbers, defined as $\mathrm{Re} = Q/(vw)$, are $0 < \mathrm{Re} < 15\,000$. Figure 5 shows the measured values of

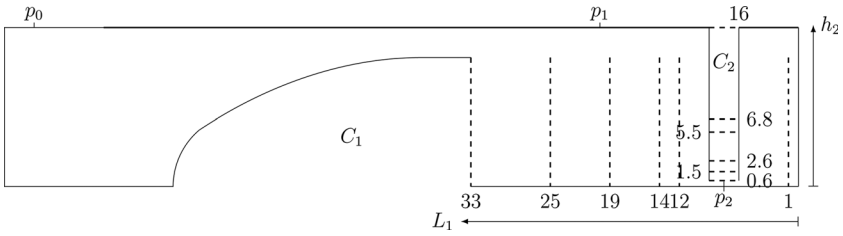

FIG. 4. Illustration of assessed geometrical configurations for different values of L_1 [mm] (dashed vertical lines) and h_2 [mm] (dashed horizontal lines) and the position of the pressure taps (p_0,p_1,p_2).

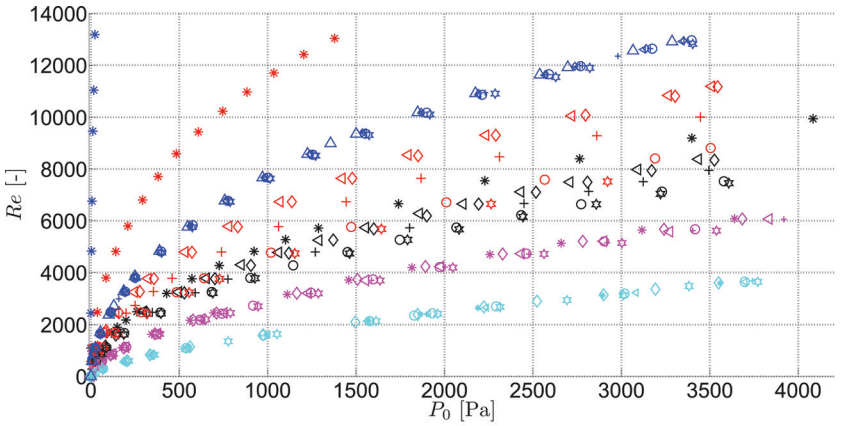

(a) $Re(P_0)$

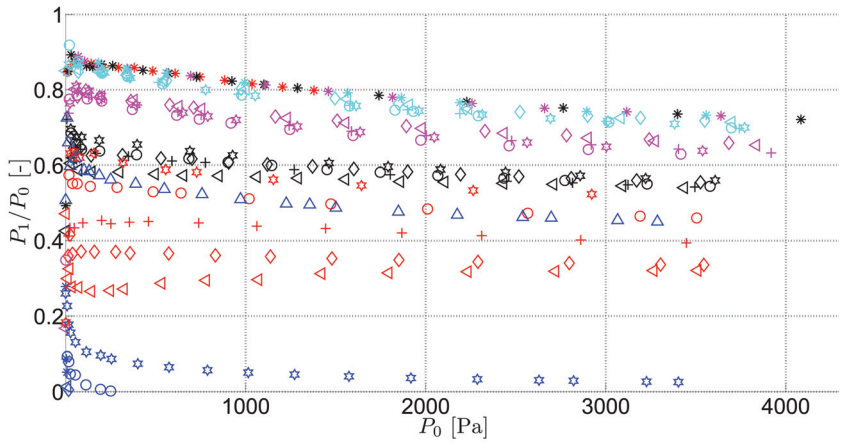

(b) $P_1/P_0(P_0)$

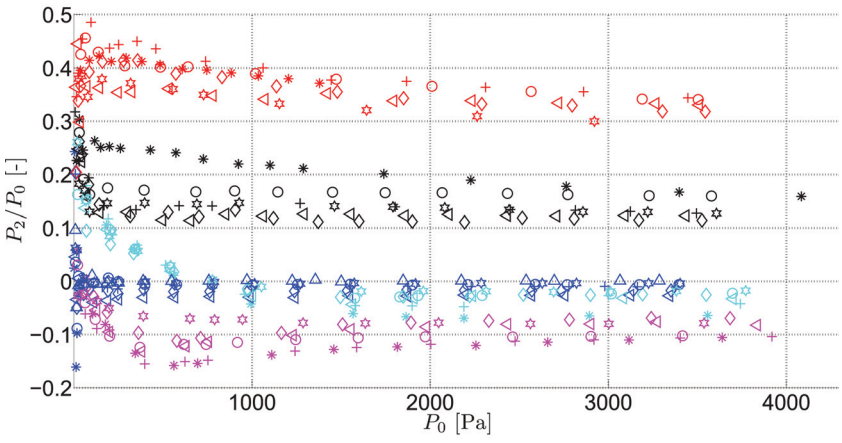

(c) $P_2/P_0(P_0)$

FIG. 5. (Color online) Overview of experimental results of Re(P_0), $P_1/P_0(P_0)$ and $P_2/P_0(P_0)$ for all assessed geometrical (L_{01},h_2) and flow (P_0) configurations: absence of the upstream obstacle C_1 is indicated as L_1 = none (*), $L_1 = 33$ (◁), $L_1 = 25$ (◇), $L_1 = 19$ (+), $L_1 = 14$ (○), $L_1 = 12$ (☆), $L_1 = 1$mm (Δ), $h_2 = 16$ (blue), $h_2 = 6.8$ (red), $h_2 = 2.6$ (black), $h_2 = 1.5$ (magenta), and $h_2 = 0.6$mm (cyan). Data for $h_2 = 5.5$ are not shown, but exhibit the same tendencies as the data for $h_2 = 6.8$.

Re and downstream pressures (P_1,P_2) as a function of P_0 and the geometrical parameters (L_1, h_2).

Figure 5(a) illustrates the measured relationship Re(P_0). For $h_2 = 0.6$ mm corresponding to a constriction degree of 96% the relationship Re(P_0) is seen to be nearly independent of L_1 since the relative difference is less than 5% for all assessed volume airflows. For $h_2 = 1.5$ mm the presence of both constrictions becomes notable since increasing L_1 from 12 to 33 mm slightly decreases P_0 with 8% and further to 12% in absence of C_1. This dependence on L_1 is even more important as the aperture h_2 is further increased up to 6.8 mm. The relative pressure decrease with increasing L_1 from 12 to 33 mm yields 25%, 44%, and 51% for $h_2 = 2.6$, $h_2 = 5.5$, and $h_2 = 6.8$ mm and decreases further to 38%, 78%, and 87% in absence of C_1. Consequently, the pressure drop increases when the gap between both constrictions is narrowed indicating that pressure recovery is favored in case of a wide gap between both constrictions.

In absence of C_2, i.e., $h_2 = h_0 = 16$ mm, pressure recovery is mainly determined by constriction degree of 81% due to the fixed aperture of $h_1 = 3$ mm. Consequently, varying L_1 from 33 to 1 mm results in a fairly constant pressure drop P_0 regardless the volume airflow rate. The slight pressure increase, less than 4%, for increasing L_1 is the result of a small pressure recovery in the channel. Figure 5(b) illustrates the pressure measured at p_1 normalized by the upstream pressure, P_1/P_0. As illustrated in Fig. 4, the relative position of the pressure tap p_1 with respect to the trailing edge of constriction C_1 depends on L_1. For $L_1 = 33$ and 25 mm the pressure is measured in the gap between both constrictions at 15 and 7 mm, respectively, downstream the trailing edge. For $L_1 = 19$ mm the pressure is measured 1 mm upstream of the trailing edge, whereas for $L_1 = 14$ and 12 mm the pressure tap corresponds to 4 and 6 mm upstream of the trailing edge. From Fig. 5(b) it is seen that in absence of C_1, the pressure ratio P_1/P_0 collapses to a single curve, which is independent of both h_2 and the volume airflow velocity Q. Nevertheless, the pressure loss increases with input pressure up to 30% due to friction since the friction factor is Reynolds number dependent and due to the development of entry flow in the uniform inlet portion of the channel (Van Dyke, 1970; Wilson, 1971; Kapila *et al.*, 1973). In addition, since the aspect ratio $h_0/w = 1.3$ is significantly smaller than 4, three-dimensional flow development is likely to occur (White, 1991; Schlichting and Gersten, 2000). Note that the one-dimensional models given in Sec. II are unable to account for such entry flow effects since all terms become 0, including the viscosity term (3), considering the range of Reynolds numbers under study. Changing the geometry at the entry of the channel is likely to reduce this pressure loss. Nevertheless, since the loss is independent of h_2, it is not an important issue for the present study.

Inserting constriction C_1 in absence of constriction C_2, i.e., $h_2 = h_0 = 16$ mm, increases the pressure drop compared to the unconstricted channel. For $L_1 = 1$ to $L_1 = 33$ mm the pressure tap p_1 is situated consecutively along the converging portion of C_1, at the minimum constriction and finally downstream C_1, so that the associated pressure drop is seen to increase from $\simeq$40% up to $\simeq$100%, i.e., $P_1/P_0 \approx 0$. The pressure drop, P_1/P_0, measured in presence of both constrictions C_1 and C_2 is intermediate to the previous configurations: a lower limit is reached in absence of C_1 and an upper limit in absence of C_2. As for $\mathrm{Re}(P_0)$ shown in Fig. 5(a), the influence of L_1 on pressure P_1 is most noticeable for large $h_2 > h_1 = 3$ mm, i.e., 6.8 and 5.5 mm, for which the pressure loss is seen to decrease with 12% or more as the gap L_1 becomes wider. In addition, the pressure loss P_1/P_0 measured for $h_2 > h_1 = 3$ mm is more pronounced than for smaller h_2, i.e., $h_2 \leq h_1 = 3$ mm, for which the pressure loss $P_1/P_0 \geq 0.5$. Consequently, the relative pressure drop P_1/P_0 reduces as h_2 decreases since the pressure drop across C_2 is increasing.

From the previous discussion of measured P_1/P_0 values and from the model terms presented in Sec. II, accounting for pressure recovery in the gap between both constrictions is expected to be important for h_2 in the range $h_0 > h_2 > h_1$ and much less for $h_2 < h_1$ when regarding the limited influence of L_1 for $h_2 < h_1$. As a consequence, the geometrical correction, i.e., interchanging physical height and gap width in the model geometry, in order to describe the flow direction is expected to be relevant for $h_2 < h_1$ and much less for $h_0 > h_2 > h_1$.

Figure 5(c) reports measured pressure losses P_2/P_0 observed at pressure tap p_2. The pressure drop for C_2 is most important for small apertures h_2 resulting in negative pressures for $h_2 \leq 1.5$ mm with an order of magnitude about 10% of P_0. Nevertheless, the pressure drop is more pronounced for $h_2 = 1.5$ mm than for $h_2 = 0.6$ mm. This might be due to (1) viscosity as seen from (3), (2) the strong asymmetry resulting in a downstream shift of the minimum pressure (Lagrée *et al.*, 2007), or (3) a small recirculation zone at the position p_2. Varying L_1 is seen to influence P_2/P_0 in particular for small apertures $h_2 \leq 1.5$ mm for which the presence of C_1 is seen to decrease the pressure drop for the assessed flow conditions.

B. Optimal data approximation

In this section, the aim is to verify the extent to which the mathematical expression relative to the physical model described in (2) explains the experimental observations. Therefore, the mathematical expression (2) is approximated under the assumptions $A_{si} \ll A_i$ and $\Delta P = P_{0,E}$ as the following parametrical function:

$$P_{0,E}[z_k(j)] = \sum_{k=1}^{n} a_k z_k(j)^{\alpha_k} \quad \alpha_k \leq 0, \quad a_k \geq 0, \tag{13}$$

with parameters a_k and α_k to be estimated by minimizing the mean square error (see Appendix B). For a fixed value of volume flow rate Q, variables $z_k(j)$ are defined from the jth measured values of geometrical experimental parameters as: $z_1(j) = h_2(j)$, $z_2(j) = h_1(j)$ and $z_3(j) = L(j)$. The number of terms n included in the summation varies from 1 to 3 as function of the number of geometrical experimental parameters taken into account. As one can see, for each individual geometrical variable, expression $a_k z_k(j)^{\alpha_k}$ is similar to model (2) under the assumptions $A_{si} \ll A_i$ and $\Delta P = P_{0,E}$.

From the estimated parameter set $\{\hat{a}_k, \hat{\alpha}_k\}_{1 \leq k \leq n} = f[\{P_0(j), z_k(j)\}_{1 \leq j \leq N}]$, with $P_0(j)$ the jth measured pressure and N the number of measurements, provided by minimization of the mean square error (Appendix B), an estimation $\hat{Q}$ of the measured volume flow rate Q is obtained as

$$\hat{Q} = w\left(\frac{2\hat{a}_1}{\rho}\right)^{-1/\hat{\alpha}_1}. \tag{14}$$

The relative errors of the estimated volume airflow rate $\hat{Q}$, expressed as $100|(\hat{Q}/Q) - 1|$, are illustrated in Fig. 6 for n set to 1, 2, and 3. Accounting for geometrical variable h_1 in addition to h_2 decreases the error percentage below 100% [Fig. 6(b)]. The error percentage is seen to reduce further by about 40% [Fig. 6(c)] when including L ($L = L_1 - 9$ mm) as a geometrical variable. Therefore, accounting for the 3 geometrical variables (h_2,h_1,L) enables to get a satisfactory estimation of the volume airflow rate Q by (14).

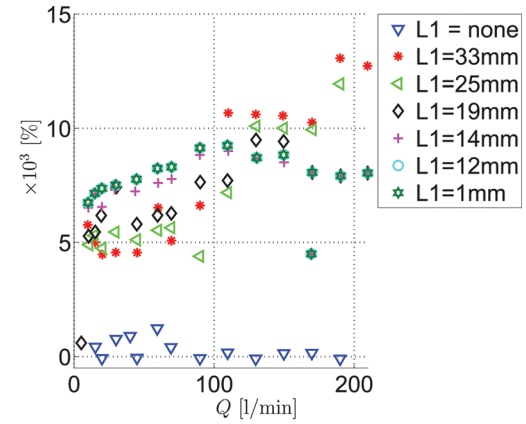

(a)$n = 1$

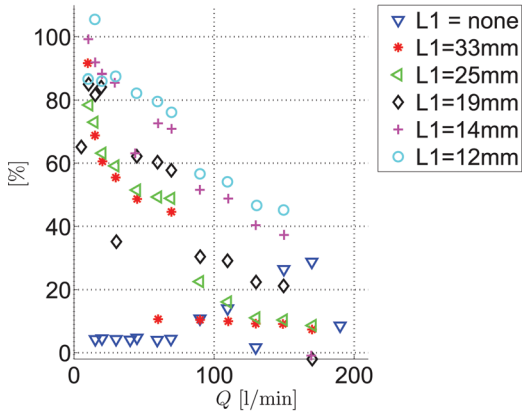

(b)$n = 2$

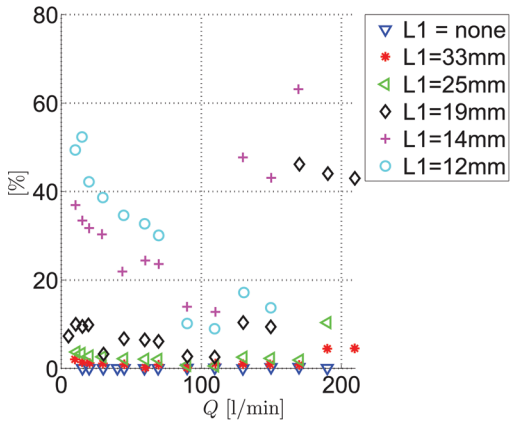

(c)$n = 3$

FIG. 6. (Color online) Relative error [%] of the estimated volume airflow rate $\hat{Q}$ as function of L_1 for (a) $n = 1$ with $z_1 = h_2$, (b) $n = 2$ with $z_1 = h_2$ and $z_2 = h_1$, and (c) n = 3 with $z_1 = h_2$, $z_2 = h_1$ and $z_3 = L$. $L_1 =$ none indicates absence of the upstream obstacle C_1.

Since the simple mathematical expression (13) is derived on a simple model structure presented in Sec. II, it is expected that discussed models are able to explain the measured data. In addition, this optimization approach provides a minimum mean square error and is therefore a reference for the error range that results from applying the physical model terms described in Sec. II. The differences between estimated parameters $\hat{a}_k$ and $\hat{\alpha}_k$ and the corresponding values identified from Bernoulli term (2) as

$$\alpha_k = -2, a_k = \frac{Q^2\rho}{2w^2} 1 \le k \le n, \tag{15}$$

reflect the need to take into account pressure losses or recovery due to, e.g., viscosity, jet formation or reattachment, which are not dealt with in Bernoulli term (2). Including additional pressure losses or recovery terms as expressed in (3)–(10) is validated in Sec. V.

V. VALIDATION OF ONE-DIMENSIONAL FLOW MODELS

The one-dimensional flow models introduced in Sec. II are validated on the measured data. It is sought to determine the model accuracy in terms of the geometrical parameters (L_1,h_2). Therefore, the pressure distribution is estimated from models taking into account different terms, (2)–(10), as discussed in Sec. II. Resulting models q and their principal features are summarized in Table III. The assessed geometry and the total pressure difference corresponding to the measured upstream pressure, i.e., assuming $\Delta P = P_0$, are model input parameters from which the volume airflow velocity and pressure distribution along the *in vitro* replica geometry, parameterized by (L_1, h_2), are estimated.

Model estimations of the volume airflow velocity and of the pressures at the positions of the pressure taps, i.e., $\hat{P}_1, \hat{P}_2$ and $\hat{Q}$, can be quantitatively compared to experimentally observed values for each set of input parameters (P_0,L_1,h_2) in order to determine the model accuracy. Consequently, the accuracy of the model estimations for $\hat{P}_1, \hat{P}_2$,and $\hat{Q}$ is sought as function of (P_0,L_1,h_2) for each model q. Relative error functions $\zeta_1^{(q)}(\hat{P}_1, P_0, L_1, h_2), \zeta_1^{(q)}(\hat{P}_2, P_0, L_1, h_2)$, and $\zeta_2^{(q)}(\hat{Q}, P_0, L_1, h_2)$ are obtained for each model, denoted by superscript q, as

$$\zeta_1^{(q)}(\hat{P}_m, P_0, L_1, h_2) = \frac{|\hat{P}_m - P_m|}{P_0}, \text{with } m \in \{1, 2\}, \tag{16}$$

$$\zeta_2^{(q)}(\hat{Q}, P_0, L_1, h_2) = \frac{|\hat{Q}_m - Q|}{Q}, \tag{17}$$

where as before P_0, P_m, and Q indicate the measured values. An error function $\bar{\zeta}_k^{(q)}$ for all $N_0(L_1, h_2)$ assessed P_0-values is defined as

$$\bar{\zeta}_k^{(q)}(\cdot, L_1, h_2) = \frac{1}{N_0}\sum_{r=1}^{N_0}\left[\zeta_k^{(q)}(\cdot, P_{0r}, L_1, h_2)\right], \tag{18}$$

TABLE III. Overview models formulated with terms (2) to (10). For each model q, the terms taken into account are indicated by ×.

	Model terms of section II					
q	(2)	(3)	(4)	(6)	(9)	terms
Ber	×					Bernoulli
Visc	×	×				viscosity
Exp			×			expansion
Con				×		contraction
Ben					×	bending

for which the summation index r in P_{0r} sums over all N_0 assessed P_0 values for each geometrical configuration (L_1,h_2) whereas $\zeta_k^{(q)}$ as well as the variable $\cdot$ are defined by (16) for $k=1$ ($\cdot=P_m$) and (17) for $k=2$ ($\cdot=Q$). From (18) the overall best mean model error $\bar{\zeta}^{(q)}(L_1,h_2)$ with respect to all assessed models q is then straightforwardly quantified as the model $\hat{q}$ minimizing the cost function $J(q)$ as expressed in (19) and (20):

$$J(q,L_1,h_2)=\frac{1}{3}(\bar{\zeta}_1^{(q)}(\hat{P}_1,L_1,h_2)+\bar{\zeta}_1^{(q)}(\hat{P}_2,L_1,h_2)+\bar{\zeta}_2^{(q)}(\hat{Q}_1,L_1,h_2), \tag{19}$$

$$\hat{q}(L_1,h_2)=\arg\min_q J(q,L_1,h_2). \tag{20}$$

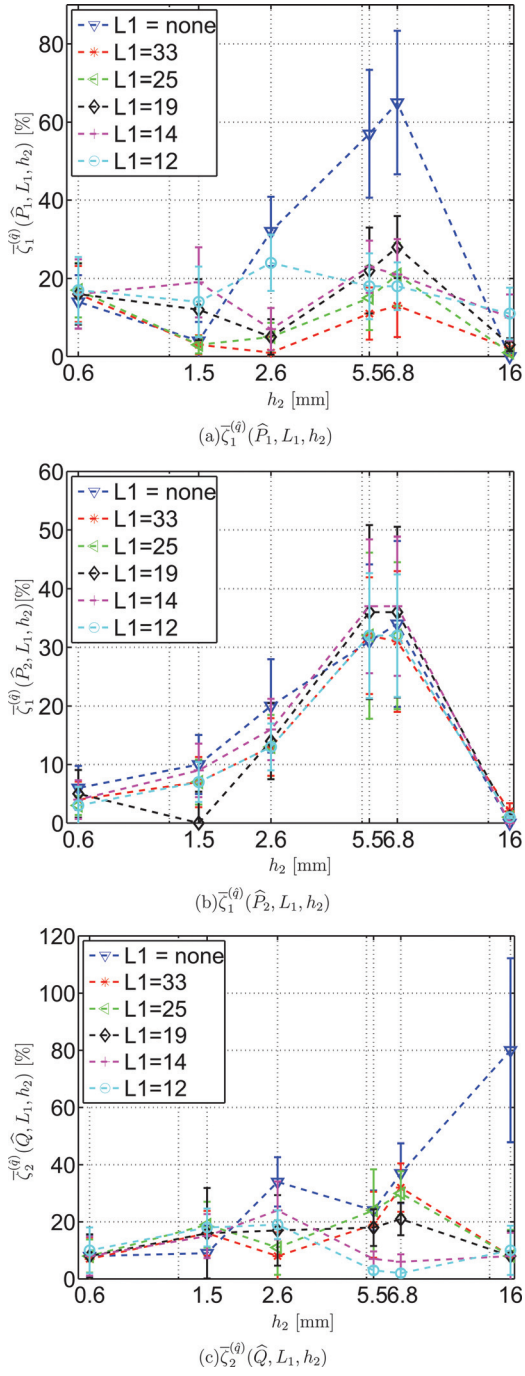

FIG. 7. (Color online) Overall best mean model error $J(\hat{q},L_1,h_2)$(19) of the models $\hat{q}(L_1,h_2)$ summarized in Table IV versus h_2 as function of L_1. Absence of the upstream obstacle C_1 is denoted $L_1=$none.

The overall best mean model errors $J(\hat{q},L_1,h_2)$ are plotted in Fig. 7. Figure 8 depicts the corresponding averaged errors $\bar{\zeta}_k^{(\hat{q})}(\cdot,L_1,h_2)$ (18) for $\hat{P}_1,\hat{P}_2$, and $\hat{Q}$. In addition to the error values (18), the error bars in Fig. 8 illustrate the sensitivity of the model accuracy for variations of the upstream pressure P_0. In general, the error sensitivity increases as the error values $\bar{\zeta}_k^{(\hat{q})}(\cdot,L_1,h_2)$ increases. The overall best mean model error yields $J(\hat{q},L_1,h_2)\leq 30\%$ for all (L_1, h_2) except in absence of C_1, denoted $L_1=$none. In absence of C_1, the errors for $h_2>1.5$ are significantly larger than in presence of C_1, so that the upper limit for the overall model accuracy increases to $J(\hat{q},L_1,h_2)\leq 50\%$. From Fig. 8 it is observed that in presence of C_1 large overall errors $J(\hat{q},L_1,h_2)$, e.g., $h_2=5.5$ compared to $h_2=1.5$ mm in Fig. 7, are due to large errors of $\bar{\zeta}_1^{(\hat{q})}(\hat{P}_2,L_1,h_2)$, and/or $\bar{\zeta}_2^{(\hat{q})}(\hat{q},L_1,h_2)$. In absence of C_1, the error $\bar{\zeta}_1^{(\hat{q})}(\hat{P}_1,L_1,h_2)$ is seen to increase as well explaining the increased overall best mean error upper limit of $J(\hat{q},L_1,h_2)\leq 50\%$ instead of $J(\hat{q},L_1,h_2)\leq 30\%$.

The models resulting in the overall best mean model error $J(\hat{q},L_1,h_2)$(19), illustrated in Fig. 7, are summarized in Table IV. From Table IV it is seen that for $h_2=16$ mm as well as $h_2=0.6$ mm accounting for viscous effects, i.e., $\hat{q}=$Visc, results in minimal errors $J(\hat{q},L_1,h_2)$ regardless the value of L_1. For intermediate values, $0.6<h_2\leq 16$, the overall best mean model errors $J(\hat{q},L_1,h_2)$ are obtained for models $\hat{q}=$Con or $\hat{q}=$Ben depending on (L_1, h_2). It is observed that inserting L_1 upstream from h_2 and moving it further downstream, i.e., decreasing L_1, causes a model shift from $\hat{q}=$Con to $\hat{q}=$Ben. So, in case of a large gap L_1 between both constrictions C_1 and C_2, the narrowed passage at C_2 can be modeled as a sudden constriction whereas for smaller L_1 the narrowed passage C_2 can be approximated as a bend in the geometry. The transition between both model approaches, i.e., constriction → bending, is seen to depend on the value of the aperture h_2. From Table IV it is seen that in presence of L_1 both small ($h_2\leq 1.5$) and large ($6.8\leq h_2$)

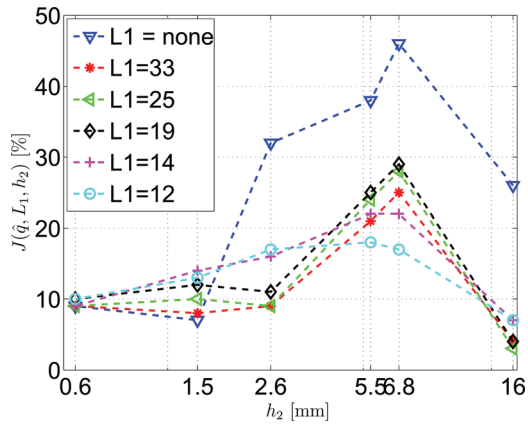

FIG. 8. (Color online) Model errors $\bar{\zeta}_k^{(\hat{q})}(\cdot,L_1,h_2)$ (18) for $\hat{P}_1,\hat{P}_2$ and $\hat{Q}$ for the models $\hat{q}(L_1,h_2)$ corresponding to $J(\hat{q},L_1,h_2)$ presented in Fig. 7 and summarized in Table IV versus h_2 as function of all assessed L_1: (a) $\bar{\zeta}_1^{(\hat{q})}(\hat{P}_1,L_1,h_2)$, (b)$\bar{\zeta}_1^{(\hat{q})}(\hat{P}_2,L_1,h_2)$, *and*(c)$\bar{\zeta}_2^{(\hat{q})}(\hat{q},L_1,h_2)$. Absence of the upstream obstacle C_1 is denoted $L_1=$none.

TABLE IV. Overview of the selected models $\hat{q}(L_1, L_2)$ resulting in the overall best mean error $J(\hat{q}, L_1, h_2)$ (19) whose value is plotted in Fig. 7. Models are referred to as outlined in Table III. For completeness also the constriction degree due to h_2 [mm], i.e., $\vartheta_2(h_2) = 1 - h_2/h_0$ [%], and the constriction degree of the gap between both constrictions due to L_1 [mm], i.e., $\vartheta_1(L_1) = 1 - (L_1 - 9)/h_0$ [%], are indicated as well.

		Decreasing L_1						
$\vartheta_1(L_1)$		0	0	0	38	69	81	
$\vartheta_2(h_2)$	h_2 \ L_1	L_1 = none	$L_1 = 33$	$L_1 = 25$	$L_1 = 19$	$L_1 = 14$	$L_1 = 12$	terms
Decreasing h_2								
0	16	Visc	Visc	Visc	Visc	Visc	Visc	viscosity
58	6.8	Con	Ben	Ben	Ben	Ben	Ben	constriction → bending
66	5.5	Con	Con	Con	Ben	Ben	Ben	constriction → bending
84	2.6	Con	Con	Con	Con	Con	Ben	constriction → bending
91	1.5	Con	Ben	Ben	Ben	Ben	Ben	constriction → bending
96	0.6	Visc	Visc	Visc	Visc	Visc	Visc	viscosity

h_2 values favors $\hat{q} = $ Ben. For intermediate h_2 values ($1.5 < h_2 < 6.8$) decreasing h_2 extend the range of $\hat{q} = $ Con in terms of decreasing L_1. Finally, we note that altering the geometry, e.g., assuming jet expansion (5), does not improve the model accuracy derived as $J(\hat{q}, L_1, h_2)$.

VI. CONCLUSION

A rigid *in vitro* replica is proposed in order to study airflow through the human vocal tract during sibilant fricative production. Two geometrical parameters are studied experimentally: the position of an upstream tongue shaped constriction in the main flow direction (L_1) and the constriction degree of a tooth shaped downstream obstacle (h_2). The shape of both obstacles is extremely simplified in order to limit the number of geometrical and flow parameters to be taken into account. Obviously, the proposed rigid replica is a severe simplification of real life physiology and several improvements can be proposed concerning (1) the shape of tongue, tooth, or/and tract and (2) extending the number of geometrical parameters.

Point pressure was measured at several streamwise locations and appeared to vary significantly over the range of imposed L_1 and h_2. In addition, varying L_1 while maintaining h_2 fixed is seen to influence the pressure at the tooth constriction. Consequently, besides h_2 (transverse tooth aperture), L_1 (streamwise tongue position) influences the resulting airflow. This is confirmed by fitting the measured pressure drop as function of imposed geometrical parameters since the accuracy of the volume flow rate estimation increases by 40% when the geometrical parameter L_1 is taken into account.

Measured pressures and volume airflow rates are compared to the outcome of one-dimensional flow models assuming a laminar incompressible irrotational and one-dimensional flow governed by Bernoulli's equation to which corrections are applied for viscosity, note that the viscosity corrections are based on Poiseuille's formula, sudden geometrical expansion, sudden geometrical constriction, and bending. In presence of the tongue shaped constriction, the accuracy for each set of geometrical parameters (L_1, h_2) expressed as a mean error for all predicted quantities and all imposed upstream pressures yields $< 30\%$. The relevance of additional corrections (resulting in the smallest errors) varies as function of (L_1,h_2). For very small ($< 58\%$) or very large ($> 96\%$) constriction degrees at the tooth the most accurate model is obtained by accounting for viscosity regardless the value of L_1. For intermediate constriction degrees, in the interval [58 96]%, narrowing the gap between both constrictions, i.e., decreasing L_1, causes the most accurate model to shift from constriction to bending. Therefore, the geometrical parameter L_1, although not explicitly appearing as a parameter in the validated one-dimensional models, does determine the appropriate corrective term for the applied cost function. In addition, it is interesting to note that the model are least accurate for tooth constriction degrees ($\approx 60\%$) for which the influence of L_1 on the measured pressures is most significant.

Consequently, one-dimensional flow models can be applied to describe the flow through the vocal tract when accounting for the relevant corrections in order to compensate, based on geometrical considerations, for the non realistic assumption of a laminar and irrotational flow. This way the approach of one-dimensional flow modeling, commonly used in physical phonation models, can be extended to the vocal tract.

Several topics for further research can be formulated. With respect to modeling, more complex flow modeling is motivated in order to describe the influence of the geometrical parameter L_1. In addition, further flow and acoustic experimental characterization needs to be assessed either qualitatively (flow visualization) or/and quantitatively (Particle Image Velocimetry, anemometry, microphone).

APPENDIX A: VISCOSITY CORRECTION TERM

Under the assumptions of two-dimensional, steady and parallel flow, i.e., Poiseuille flow between two parallel plates (White, 1991), the viscid Euler equation, describing the relationship between local velocity u and driving pressure P, reduces to

$$\mu \frac{d^2u}{dy^2} = \frac{dP}{dx}. \tag{A1}$$

The local velocity $u(y)$ is then easily derived as function of the pressure difference dP/dx and the height between the

parallel plates $h(x)$ so that after some calculus the mean velocity $U(x)$ follows

$$U(x) = -\frac{1}{12\mu}\frac{dP}{dx}h(x)^2. \tag{A2}$$

Introducing volume flow rate $Q = U(x)A(x)$ and assuming a rectangular area with constant width w, $A(x) = h(x)w$, leads straightforwardly to

$$dP = \frac{12\mu Q}{w}\frac{1}{h(x)^3}dx, \tag{A3}$$

so that Eq. (3) follows immediately:

$$\Delta P = -\frac{12\mu Q}{w}\int_{x_i}^{x_{si}}\frac{1}{h(x)^3}dx. \tag{A4}$$

APPENDIX B: PARAMETER ESTIMATION

The parameters a_k and α_k defined in Sec. IV B are estimated in a least square sense from the experimentally measured $P_0(j)$ data described in Sec. IV A and geometrical variables (h_2, h_1, L) as shown in Sec. III and Fig. 3. Therefore, the criterion is defined as

$$J(\{a_k, \alpha_k\}_{1\le k\le n}) = \frac{1}{N}\sum_{j=1}^{N}\left|P_0(j) - P_{0,E}(j)\right|^2,$$

with N the number of measured upstream pressures $P_0(j)$ for fixed volume flow rate Q. Parameters estimation is thus obtained by

$$\{\hat{\alpha}_k, \hat{a}_k\}_k = \arg\min_{\{a_k,\alpha_k\}_k} \mathrm{J}\left(\{a_k,\alpha_k\}_{1\le k\le n}\right). \tag{B1}$$

The steepest gradient method (Avriel, 2003) is applied to solve the optimization problem resulting in the sought parameter estimation $\{\hat{a}_k, \hat{\alpha}_k\}_{1\le k\le n} = f[P_0(j), z_k(j)]_{1\le j\le N}$.

ACKNOWLEDGMENTS

Financial support of the Agence Nationale de la Recherche (ANR-07-JCJC-0055) is gratefully acknowledged.

Adachi, S., and Honda, K. (**2003**). "CFD approach to fricative sound sources," in *Proc. 6th International Seminar on Speech Production* (Sydney, Australia), pp. 1–4.
Avriel, M. (**2003**). *Nonlinear Programming: Analysis and Methods* (Dover Publishing, New York), p. 548.
Barney, A., Shadle, C., and Davies, P. (**1999**). "Fluid flow in a dynamic mechanical model of the vocal folds and tract. I. measurements and theory," J. Acoust. Soc. Am. **105**, 444–455.
Blevins, R. (**1992**). *Applied Fluid Dynamics Handbook* (Krieger Publishing Company, Malabar), p. 570.
Bodony, D. (**2005**). *The Prediction and Understanding of Jet Noise* (Center for Turbulence Research Annual Research Briefs, Stanford University, Palo Alto, CA), pp. 367–377.
Cisonni, J., Van Hirtum, A., Pelorson, X., and Willems, J. (**2008**). "Theoretical simulation and experimental validation of inverse quasi one-dimensional steady and unsteady glottal flow models," J. Acoust. Soc. Am. **124**, 535–545.
Daniloff, R., Schuckers, G., and Feth, L. (**1980**). *The Physiology of Speech and Hearing* (Prentice-Hall, New York), p. 454.
Fant, G. (**1960**). *The Acoustic Theory of Speech Production* (Mouton, Hague, Netherlands), p. 328.
Hirano, M. Yoshida, T., and Kurita, S. (**1987**). "Anatomy and behavior of the vocal process," in *Laryngeal Function in Phonation and Respiration*, edited by T. Baer, C. Sasaki, and K. Harris (College Hill Press, Boston, MA), pp. 1–13.
Howe, M., and McGowan, R. (**2005**). "Aeroacoustics of [s]," Proc. Roy. Soc. A **461**, 1005–1028.
Ishizaka, K. and Flanagan, J. (**1972**). "Synthesis of voiced sounds from a two-mass model of the vocal cords," Bell Syst. Tech. J. **51**, 1233–1267.
Kapila, A., Ludford, G., and Olunloyo, V. (**1973**). "Entry flow in a channel. Part 3. Inlet in a uniform stream," J. Fluid Mech. **57**, 769–784.
Krane, M. (**2005**). "Aeroacoustic production of low-frequency unvoiced speech sounds," J. Acoust. Soc. Am. **118**, 410–427.
Kundu, P. (**1990**). *Fluid Mechanics* (Academic Press, London), p. 759.
Lagée, P., Van Hirtum, A., and Pelorson, X. (**2007**). "Asymmetrical effects in a 2D stenosis," Eur. J. Mech. B/Fluids **26**, 83–92.
Lous, N., Hofmans, G., Veldhuis, N., and Hirschberg, A. (**1998**). "A symmetrical two-mass vocal-fold model coupled to vocal tract and trachea, with application to prosthesis design," Acta Acust. **84**, 1135–1150.
Magne, P., Gaulluci, G., and Belser, U. (**2003**). "Anatomic crown width/length ratios of unworn and worn maxillary teeth in white subjects," J. Prosthet. Dent. **89**, 453–461.
Narayanan, S., Alwan, A., and Haker, K. (**1995**). "An articulatory study of fricative consonants using magnetic resonance imaging," J. Acoust. Soc. Am. **98**, 1325–1347.
Nozaki, K., Akiyama, T., Shimojo, S., Maeda, S., and Tamagawa, H. (**2005**). "Integration of computational fluid dynamics and computational aero acoustics on grid for dental applications," in *Proc. 18th IEEE Symposium on Computer-Based Medical Systems*, Ann Arbor, MI, pp. 517–522.
Pelorson, X., Hirschberg, A., Van Hasselt, R., Wijnands, A., and Auregan, Y. (**1994**). "Theoretical and experimental study of quasisteady-flow separation within the glottis during phonation. Application to a modified two-mass model," J. Acoust. Soc. Am. **96**, 3416–3431.
Ramsay, G. (**2008**). "The influence of constriction geometry on sound generation in fricative consonants," in *Proc. Acoustics 08*, Paris, France, pp. 1–4
Rudolph, D., Dominguez, P., Ahn, K., and Thinh, T. (**1998**). "The use of tooth thickness in predicting intermaxillary tooth-size discrepancies," Angle Orthod. **68**, 133–140.
Runte, C., Lawerino, M., Dirksen, D., Bollmann, F., Lamprecht-Dinnesen, A., and Seifert, E. (**2001**). "The influence of maxillary central incisor position in complete dentures on/s/sound production," J. Prosthet. Dent. **85**, 485–495.
Ruty, N., Pelorson, X., Van Hirtum, A., Lopez, I., and Hirschberg, A. (**2007**). "An in-vitro setup to test the relevance and the accuracy of low-order vocal folds models," J. Acoust. Soc. Am. **121**, 479–490.
Schlichting, H., and Gersten, K. (**2000**). *Boundary Layer Theory* (Springer Verlag, Berlin), p. 801.
Shadle, C. (**1985**). "The acoustics of fricative consonants," Ph.D. thesis, Dept. Electrical Engineering, Massachusetts Institute of Technology, Cambridge, MA.
Shadle, C. (**1991**). "The effect of geometry on source mechanisms of fricative consonants," J. Phonetics **19**, 409–424.
Shadle, C., Berezina1, M., Proctor, M., and Iskarous, K. (**2008**). "Mechanical models of fricatives based on MRI-derived vocal tract shapes," in *Proc. 8th International Seminar on Speech Production*, Strasbourg, France, pp. 417–420.
Sinder, D. (**1999**). "Speech synthesis using an aeroacoustic fricative model," Ph.D. thesis, Dept. Electrical and Computer Engineering, Rutgers State Universtiy of New Jersey, Newark, NJ.
Stevens, K. (**1998**). *Acoustic Phonetics*, MIT Press, London, p. 628.
Van Dyke, M. (**1970**). "Entry flow in a channel," J. Fluid Mech. **44**, 813–823.
Van Hirtum, A., Cisonni, J., and Pelorson, X. (**2009a**). "On quasi-steady laminar flow separation in the upper airways," Commun. Numer. Meth. Eng. **25**, 447–461.
Van Hirtum, A., Grandchamp, X., and Pelorson, X. (**2009b**). "Moderate Reynolds number axisymmetric jet development downstream an extended conical diffuser: Influence of extension length," Eur. J. Mech. B/Fluids **28**, 753–760.
Van Hirtum, A., Grandchamp, X., Pelorson, X., Nozaki, K., and Shimojo, S. (**2010**). "Large Eddy Simulation and 'in-vitro' experimental validation of flow around a teeth-shaped obstacle," Int. J. Appl. Mech. **2**, 265–279.
White, F. (**1991**). *Viscous Fluid Flow*, McGraw-Hill, New York, p. 640.
Wilson, S. (**1971**). "Entry flow in a channel. Part 2," J. Fluid Mech. **46**, 787–799.